Evidence of Microporous Carbon Nanosheets Showing Fast Kinetics in both Gas Phase and Liquid Phase Environments

*Zhen-Yu Jin, Yuan-Yuan Xu, Qiang Sun, and An-Hui Lu**

***D**espite the great advantages of microporous carbons for applications in gas phase separation, liquid phase enrichment, and energy storage devices, direct experiment data and theoretical calculations on the relevance of properties and structures are quite limited. Herein, two model carbon materials are designed and synthesized, i.e., microporous carbon nanosheets (MCN) and microporous carbon spheres (MCS). They both have nearly same composition, surface chemistry, and specific surface area, known morphology, but distinguishable diffusion paths. Based on these two types of materials, a reliable relationship between the morphology with different diffusion paths and adsorption kinetics in both gas phase and liquid phase environments is established. When used for CO_2 capture, MCN shows a high saturated CO_2 capacity of 8.52 μmol m^{-2} and 18.4 mmol cm^{-3} at 273 K and ambient pressure, and its calculated first-order rate constant is ≈7.4 times higher than that of MCS. Moreover, MCN shows a quick and high uptake of Cr (VI) and a higher-rate performance for supercapacitors than MCS does. These results strongly confirm that MCN exhibits improved kinetics in gas phase separation, liquid phase enrichment, and energy storage devices due to its shorter diffusion paths and larger exposed geometrical area resulting from the nanosheet structure.*

1. Introduction

Microporous carbon materials have received significant attention because of their excellent physicochemical properties of large surface area, narrow pore size distribution, good electrical conductivity, versatile forms, and excellent acid and alkali corrosion resistance.[1–5] These outstanding features enable them to be ideal candidates for use in gas separation,[6–9] water treatment,[10,11] and energy storage.[12–14] From universal point of view, the higher micropore surface area the carbon has, the higher adsorption or storage capacity could be achieved. However, the conflicting conclusions were also reported from time to time. It is because conventional microporous carbons commonly face one major challenge, i.e., adsorption kinetics is limited by the intrinsic internal diffusion resistance caused by their large particle size in three dimensions.[15–20] To address this, recent approaches to construct carbon structures with reduced dimensions down to the nanometer scale have been used by researchers.[21–25] It is worth noting that improved adsorption kinetics should be dependent on the shorter diffusion paths of microporous carbon structures. Nevertheless, direct experiment data and theoretical calculations on the relevance this to the properties are quite limited, because of the difficulty in simultaneously achieving microporous carbon models having distinguishable diffusion paths and porosity, but with similar composition, surface chemistry and specific surface area, for the purpose of precise study.

Z.-Y. Jin, Y.-Y. Xu, Dr. Q. Sun, Prof. A.-H. Lu
State Key Laboratory of Fine Chemicals
School of Chemical Engineering
Dalian University of Technology
Dalian 116024, P. R. China
E-mail: anhuilu@dlut.edu.cn

DOI: 10.1002/smll.201501692

In recent years, our group and others have made progress in the structural-controlled synthesis of porous carbons with defined morphologies, dimensions and tunable pore sizes, particularly in spherical carbons[26–28] and sheet-structured carbons.[21–24,29] This knowledge allows us to synthesize microporous carbon model materials using the same precursors and achieve controllable morphologies (carbon nanosheets and carbon spheres). Thus, a reliable relationship between the carbon morphology with different diffusion paths and its adsorption kinetic performance for CO_2 capture, Cr (VI) removal and supercapacitors in aqueous system can be established in all probability. The results indicate that sheet structures are ideal for quick response applications in gas and liquid phase environments.

2. Results and Discussion

Microporous carbon nanosheets (MCN) and spheres were synthesized using the procedure presented in the experimental section. Briefly, after dissolving 1-butyl-3-methylimidazolium imidazolide ionic liquid, resorcinol and formaldehyde in deionized water, the solution was cured at 90 °C for 24 h. The synthesized polymer was dried and then carbonized at 800 °C. Consequently, carbon products with a spherical morphology were obtained, with the spherical units having an average diameter of 4.0 ± 0.5 μm, as shown in the scanning electron microscope (SEM) image of **Figure 1**a. When using graphene oxide (GO) as an additive, the prepared carbon products have a sheet-like structure with a smooth surface. The material has graphene as an inner plate and carbon as an outer coating layer (Figure 1b,c). The average thickness of the carbon sheets is measured as 128 ± 4 nm. This strongly indicates the sheet-structure directing effect of GO. As seen in Figure 1d, the transmission electron microscopy (TEM) image of MCN also clearly shows a thin and smooth sheet nanostructure and curved edges.

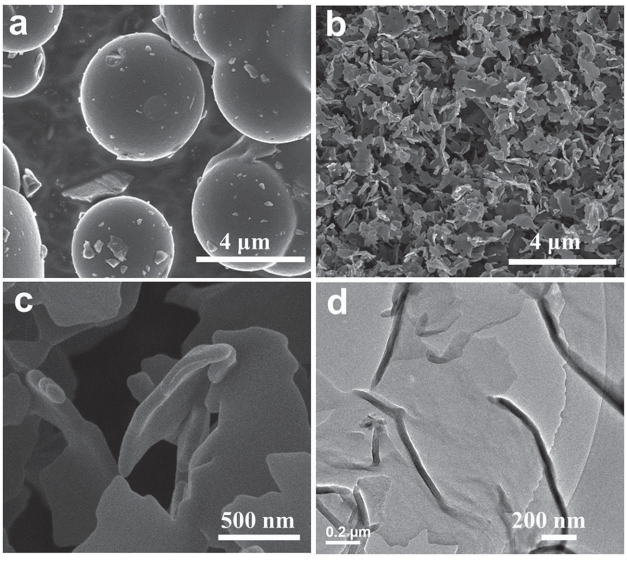

Figure 1. a) SEM image of microporous carbon spheres, b,c) SEM images, and d) TEM image of microporous carbon nanosheets.

The porous properties of the resulting microporous carbon spheres (MCS) and MCN materials were analyzed by nitrogen sorption measurements at 77.4 K. As shown in **Figure 2**a, the nitrogen adsorption isotherms of both MCS and MCN show a type I curve, indicating a permanent microporosity. The two isotherms are almost identical, indicating that these two samples have similar pore structures. Indeed, the Brunauer–Emmett–Teller (BET) surface areas are 720 $m^2\ g^{-1}$ for MCN and 710 $m^2\ g^{-1}$ for MCS and the micropore specific surface areas are 647 $m^2\ g^{-1}$ for MCN and 646 $m^2\ g^{-1}$ for MCS. Pore volumes are 0.38 $cm^3\ g^{-1}$ for MCN and 0.35 $cm^3\ g^{-1}$ for MCS. The pore size distribution curves of the two samples show a sharp peak centered at 5.4 Å as shown in Figure 2b. Furthermore, it is remarkable that MCS and MCN both have an amorphous carbon skeleton and very similar surface functional groups. This has been confirmed by X-ray diffraction (XRD) analysis (Figure 2c), Raman spectra (Figure 2d), and Fourier transform infrared spectroscopy spectra (Figure S1, Supporting Information). All in all, these results suggest that MCS and MCN are carbon materials with quite similar pore structures and amorphous features, which thus minimize the influence of other variable factors and provide a suitable model to investigate the relevance of morphology to adsorption kinetics.

In order to clarify the influence of morphology with different diffusion paths on the gas phase adsorption behavior, CO_2 adsorption kinetics were measured at 298 K and 1 bar (Part I, Supporting Information). As shown in **Figure 3**a, it can be seen that the capacity rise to 3.07 mmol g^{-1} is completed within 10 min over MCN. By contrast, the capacity rise of MCS is slower, and a longer time of about 30 min is needed to reach the maximum capacity (2.34 mmol g^{-1}), where the calculated rate constant (Figure 3b) of MCN is ≈7.4 times higher than that of MCS. These results clearly suggest that MCN is more favorable for the diffusion of CO_2 molecules from the surface into the inner pores of the sorbent due to its remarkable short diffusion path and larger calculated exposed geometrical area derived from the sheet structure. The estimated geometrical surface area of MCN is 10.4 times that of MCS and the detailed calculation is summarized in Part II (Supporting Information). When the temperature was increased to the range 40–70 °C, desorption processes take place on the two carbon sorbents (Figure 3a). Much rapid desorption is obtained and more absorbed CO_2 molecules are desorbed when the temperature of the MCN adsorbent was raised to 70 °C, demonstrating the possibility for CO_2 capture by temperature swing adsorption. The measured thermal conductivities of MCN and MCS are 1.78 and 0.24 W $K^{-1}\ m^{-1}$, respectively, with former about seven times the latter. Thus, the good desorption performance of MCN can be ascribed to its short diffusion path and high thermal conductivity.

Under ambient pressure, MCN shows a high saturated CO_2 capacity of 27.1 wt% (6.18 mmol g^{-1}), 24.2 wt% (5.51 mmol g^{-1}) and 15.5 wt% (3.51 mmol g^{-1}) at temperatures of 243, 273, and 298 K (Figure 3c), respectively. The calculated separation ratio and Henry's law selectivity of CO_2/N_2 are accordingly 11.3 and 45, at the temperature of 298 K (Figure 3d). The results are comparable to and even superior to those reported for

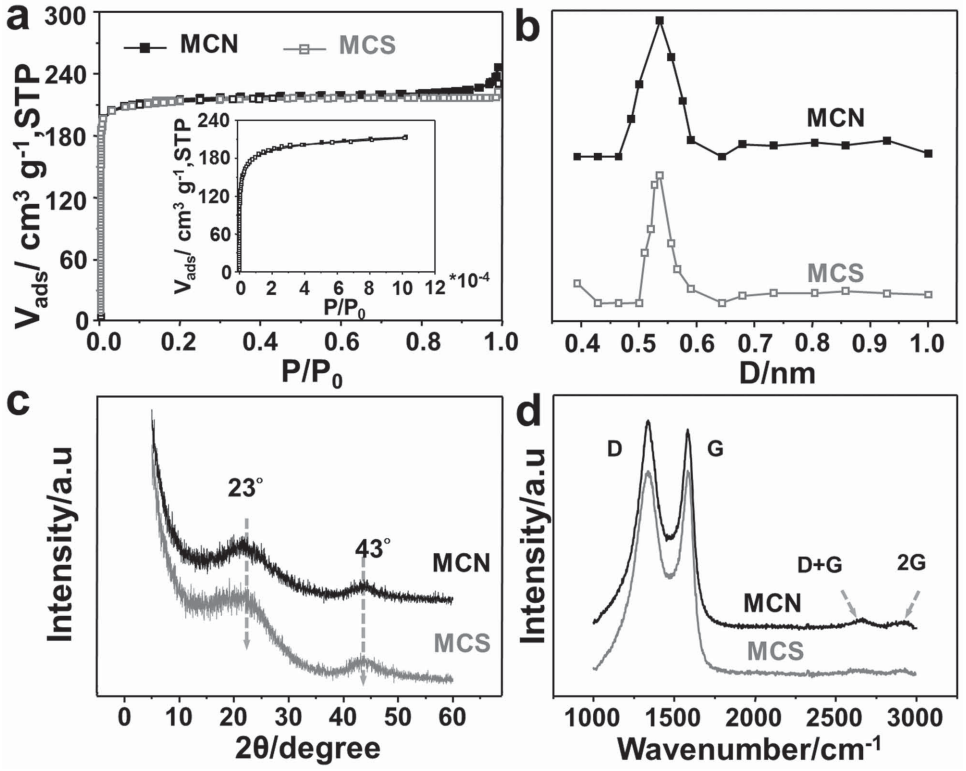

Figure 2. a) N_2 sorption isotherms, b) pore size distributions calculated using the NLDFT method, c) XRD patterns, and d) Raman spectra of MCN and MCS.

solid sorbents including carbon, zeolites, polymers, and MOFs (Table S1, Supporting Information). Notably, the calculated and normalized capacities of 8.52 μmol m^{-2} (i.e., 5.0 CO_2 molecules nm^{-2}) and 18.4 mmol cm^{-3} at 273 K and ambient pressure are extremely high and indeed are one of the highest reported to date among various widely used microporous solid materials with specific surface areas greater than 1000 m^2 g^{-1} (Figure 3e and Table S2, Supporting Information).[15,30–34] Such a high utilization of surface area and large amount of CO_2 captured by MCN reflect high permeability caused by the short diffusion paths. Moreover, repeated CO_2 cyclic adsorption measurements show no noticeable change and demonstrate good recyclability of MCN. As seen in Figure 3f, the dynamic "breakthrough" experiments clearly demonstrate that MCN can completely separate CO_2 from an N_2/CO_2 gas mixture, and the captured CO_2 can be quickly desorbed when the gas carrier is switched to argon at 298 K (Figure S2a, Supporting Information), supporting the idea of using MCN as a selective and reversible CO_2 reservoir against nitrogen. In fact, >95% of its intrinsic CO_2 uptake is desorbed within 3 min under such mild regeneration conditions and further cycling does not lead to visible fading of kinetics and capacity (Figure S2b, Supporting Information).

To further investigate whether MCN can show good adsorption kinetics in the liquid phase, Cr (VI) removal from acid aqueous solutions (pH = 3) was carried out at an initial concentration of 5 mg L^{-1} using the 1,5-diphenylcarbazide method.[35] As shown in **Figure 4**a, MCN shows quick and high uptake of Cr (VI) compared to MCS under identical liquid phase adsorption conditions. The normalized values of chromium ions adsorbed with respect to the specific surface area of MCN and MCS are accordingly 0.7 and 0.47 μg m^{-2}, again indicating a higher surface utilization of MCN. It is worth noting that good wettability is helpful for the removal of Cr (VI) (Figure S3, Supporting Information). The adsorption kinetics of the two samples were fitted by a pseudo-second-order model given in Part III in the Supporting Information and Figure 4b,c. The calculated rate constant of MCN (9.2×10^{-3} g mg^{-1} min^{-1}) is 6.6 times higher than that of MCS (1.4×10^{-3} g mg^{-1} min^{-1}), demonstrating the improved adsorption kinetics of the sheet structure.

Considering the highly desired electrolyte ion penetration or mobility in the pore structure of a microporous carbon based supercapacitor electrode, a three-electrode system was used to evaluate the electrochemical properties of the MCN for supercapacitors. As shown in Figure 4d and Figures S4 and S5 (Supporting Information), MCN showed a high-rate performance and a capacitance retention ratio of 79.6% compared to the initial capacitance over a wide range of current densities from 0.5 to 20 A g^{-1}, highlighting excellent suitability for high-rate operation. Thus, the excellent rate performance of MCN can be attributed to short diffusion paths for electrolyte ion transport.

3. Conclusion

Microporous carbon nanosheets and spheres were prepared using the same precursors and show quite similar porous structures, specific surface areas, and amorphous features.

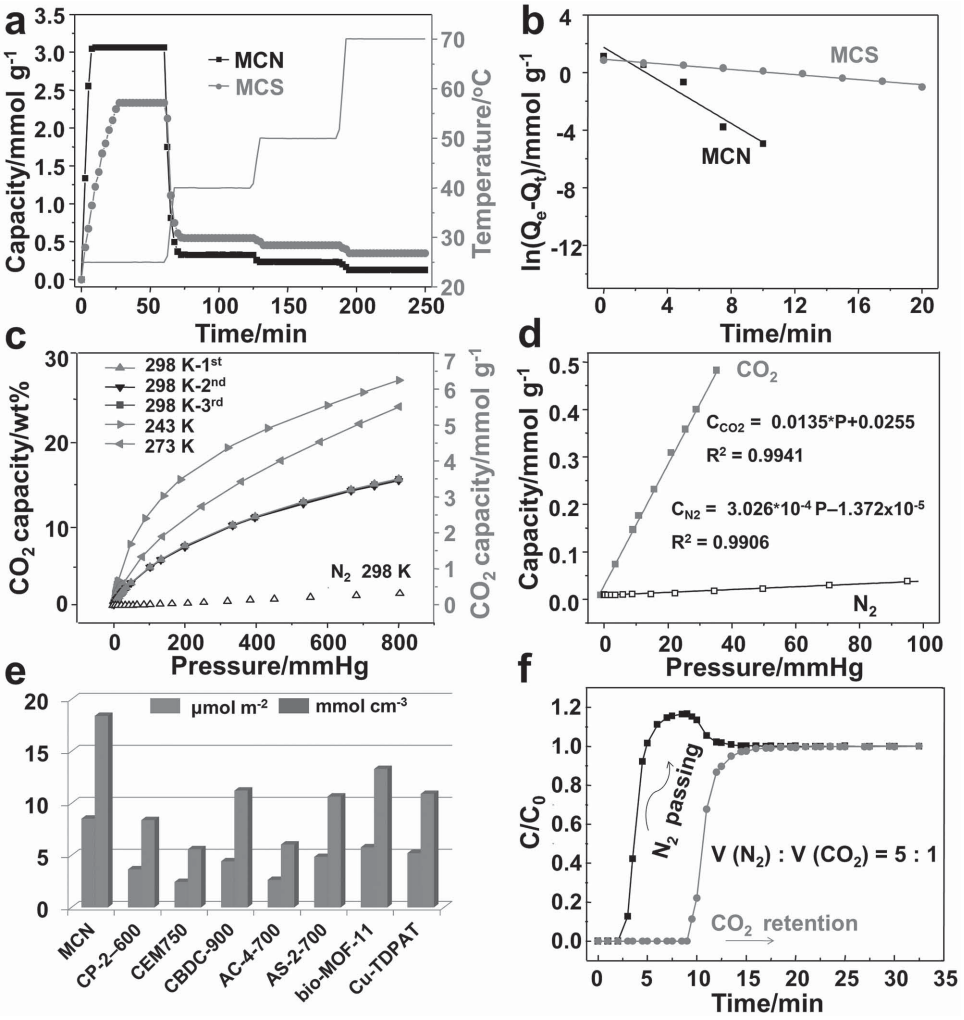

Figure 3. a) Time-resolved CO_2 adsorption–desorption of MCN and MCS at 298 K and 1 bar, b) first-order linear plot of the CO_2 adsorption for MCN and MCS, c) CO_2 and N_2 adsorption isotherms of MCN at different temperatures and ambient pressure, d) enlargement of the initial stage of CO_2 and N_2 isotherms at 298 K of MCN, e) capacity comparison of MCN and some reported microporous solid sorbents with high specific surface area, and f) breakthrough curves of a mixed stream of N_2:CO_2 = 5:1 (v/v) at 298 K.

Such controlled model materials allow us to deduce a reliable relationship between morphology with different diffusion paths and the potential practical application of microporous carbon. The results strongly confirm that microporous carbon nanosheets exhibit improved kinetics in gas phase separation, liquid phase enrichment, and energy storage devices, due to their shorter diffusion paths and larger exposed geometrical area derived from the nanosheet structure.

4. Experimental Section

Chemicals: *n*-Butyl bromide, 1-methylimidazole, imidazole, sodium hydroxide (NaOH), methanol (MeOH), diethyl ether, and ethanol were supplied by Sinopharm Chemical Reagent Co., Ltd. Resorcinol (R) and formaldehyde (denoted by F, from formalin with a concentration of 37 wt%) were purchased from Tianjin Kermel Chemical Reagent Co., Ltd. All chemicals used were analytical reagent grade. Unless otherwise specified, all chemicals were used as received.

Material Synthesis: GO was synthesized from natural graphite powder by the modified Hummers method.[36] A GO suspension was obtained under ultrasonication for at least 4 h before use. For MCN synthesis: 0.122 g 1-butyl-3-methylimidazolium imidazolide ionic liquid was dissolved in 6.5 mL GO colloids (1.8 mg mL^{-1}) with magnetic stirring at 25 °C for 10 min. Then 1.125 g R was added to the above solution and stirred for another 10 min. Subsequently, 1.659 g F was quickly injected into the solution. The reaction mixture was stirred for another 10 min, and then was transferred into an oven at 90 °C for an additional 24 h. The sample was dried at room temperature for 24 h and then at 50 °C for 24 h to obtain the precursor. The precursor was ground to a fine powder (40–60 mesh) and then washed several times with deionized water before pyrolysis at 800 °C for 2 h under a nitrogen atmosphere. For MCS synthesis the process was identical to that of MCN except that no GO was present.

Characterization: Nitrogen-sorption experiments were performed at 77.4 K on a Micromeritics ASAP 2020 device, and prior to analysis all samples were degassed under a pressure of 0.05 mbar at 200 °C for at least 4 h. The pore size distribution below 1 nm was calculated using the nonlocal density functional theory (NLDFT) model. The BET method was used to calculate the specific surface areas (S_{BET}, P/P_0 = 0.05–0.20). Total pore volumes

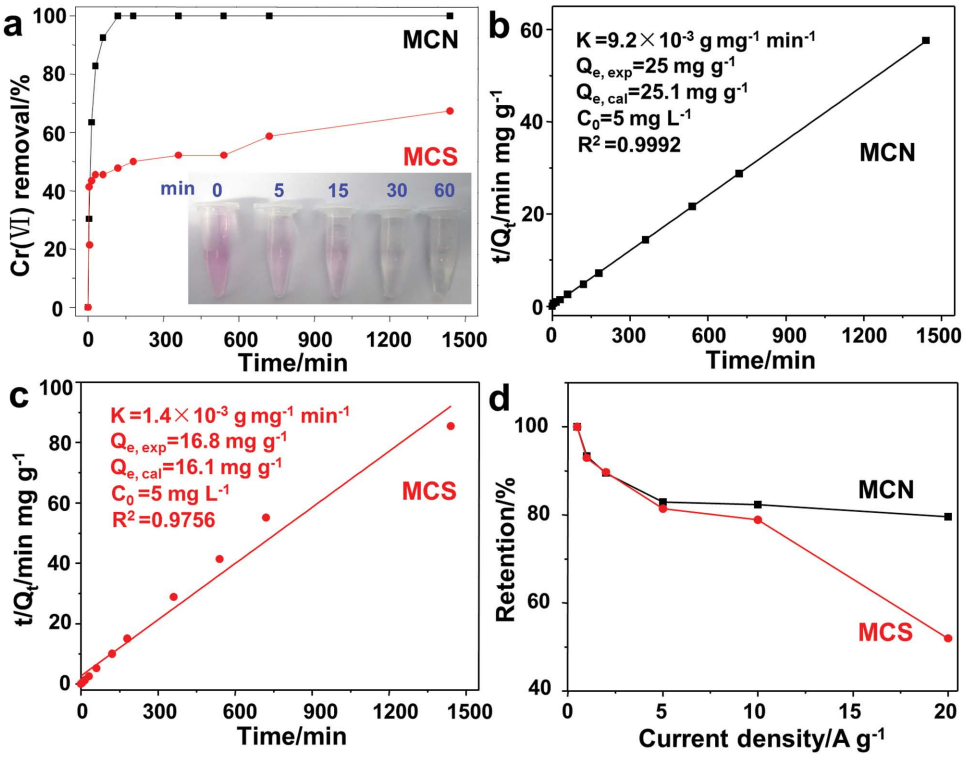

Figure 4. a) Relationship between the removal efficiency and time for the adsorption of Cr (VI) at initial concentrations of 5 mg L^{-1}. Inset photo indicates the color changes of the Cr (VI) solution using MCN as sorbent, b,c) pseudo-second-order linear plot for the removal of Cr (VI) at an initial concentration of 5 mg mL^{-1}, and d) specific capacitance retention ratios at different current densities.

(V_{total}) were calculated from the amount of nitrogen adsorbed at a relative pressure, P/P_0, of 0.99. Micropore specific surface areas (S_{micro}) and micropore volumes (V_{micro}) were obtained using the t-plot method. The morphology and structure of the samples were characterized by SEM (NOVA NanoSEM 450), TEM (FEI Technai F30), XRD (Rigaku D/Max 2400 diffractometer using Cu Kα radiation (λ = 0.15406 nm)), and Raman spectroscopy (Renishaw RM2000 Raman). The thermal conductivity was measured using a thermal conductivity detector (TCD) (Xiangtan City Instrument Co., Ltd, DRL-III). UV spectra were obtained on a UV–vis Spectrophotometer (TECHCOMP, UV-2300) and the wavelength was 540 nm.

Equilibrium Gas-Adsorption Measurements: The gas-adsorption isotherms were measured on a Micromeritics ASAP 2020 static volumetric analyzer. The gas-adsorption capacity was recorded in terms of adsorbed volume under standard temperature and pressure.

Kinetics of CO_2 Adsorption: The adsorption kinetics of CO_2 were measured on a thermogravimetric analyzer (Netzsch STA 449 F3). First, the sample (10 mg) was degassed in a stream of N_2 (50 mL min^{-1}) at 200 °C for 1 h. It was then cooled in an N_2 stream to 25 °C and exposed to a gas stream that contained CO_2 (50 mL min^{-1}) and N_2 (10 mL min^{-1}) as a protective gas. After reaching a steady state (60 min), the sample was heated stepwise to 40, 50, and 70 °C at 5 °C min^{-1} and held at each temperature for 60 min. The mass of the sorbent plus adsorbate was measured at each steady state.

Dynamic Gas-Separation Measurements: The separation of CO_2 from CO_2/N_2 binary mixtures was performed on a fixed-bed adsorber (a stainless steel tube with an inner diameter of 8 mm and a length of 130 mm) at about 1 bar and 298 K, which were controlled by a pressure controller and a thermostatic water bath, respectively. First, the bed was heated at 95 °C in Ar at a flow rate of 50 ml min^{-1} for 2 h. Then, the breakthrough experiment was performed by abruptly switching from argon to the gas mixture that contained 15% CO_2 in N_2 (v/v) with a total flow rate of 7 mL min^{-1}. The effluent gas was monitored online using an Agilent 7890A gas chromatograph with a TCD. After the effluent flow rate and the relative amounts of the effluent gases became constantan Ar flow was introduced to activate the adsorbent and then start the next round of measurements.

Cr (VI) Adsorption Experiments: Typically, 20 mg of sample was added to 100 mL solution of $K_2Cr_2O_7$ in distilled water (5 mg L^{-1}) and stirred at room temperature for 24 h in a closed vessel. The pH of the suspensions was adjusted to 3 by adding an HCl solution (0.1 M). During the adsorption process, about 0.3 ml of the Cr (VI) solution was extracted with a needle tube equipped with a membrane filter at different times and then diluted to be used for colorimetric measurements. The obtained solutions were determined using the 1,5-diphenylcarbazide method.[35] The solution concentration was determined by UV–vis spectrophotometry at 540 nm.

Electrode Preparation: The working electrode was prepared by mixing 85 wt% active material and 15 wt% polytetrafluoroethylene (PTFE) in 7 mL ethanol, followed by ultrasonication for 20 min. A slurry of the mixture was rolled into a film, cut into a suitable shape, and placed in an oven at 150 °C for 6 h, followed by placing it on a nickel foam current collector. Both cyclic voltammetry (CV) and galvanostatic charge/discharge cycling (GC) measurements were carried out at room temperature with a conventional three-electrode electrochemical setup, in which the active material served as the working electrode and a Pt plate and Hg/HgO were

used as the counter electrode and reference electrode, respectively. A 6 M KOH aqueous solution was used as the electrolyte. The capacitive performance of the cells was determined using a CHI660D electrochemical workstation (CH Instruments Inc., Shanghai, China) at 25 °C. CV and GC were used to evaluate the electrochemical performance of the electrodes. Stability measurements were carried out using a multichannel electrochemical workstation (Arbin Instruments USA). The specific capacitance of one electrode (C) was calculated from the discharge process after 20 cycles of activation, according to the following formula:

$$C = \frac{I\Delta t}{\Delta V} \quad (1)$$

where I (A g^{-1}) is the discharge current density based on the total mass of active material in the two electrodes, Δt (s) is the discharge time, and ΔV (V) is the potential window from the end of the internal resistance (R) drop to the end of the discharge process.

Supporting Information

Supporting Information is available from the Wiley Online Library or from the author.

Acknowledgements

This work was supported by the NSFC (Grant Nos. 21225312 and 21473021) and the Ph.D. Programs Foundation of Ministry of Education of China (20120041110019).

[1] H. Nishihara, T. Kyotani, *Adv. Mater.* **2012**, *24*, 4473.
[2] A. Stein, Z. Wang, M. A. Fierke, *Adv. Mater.* **2009**, *21*, 265.
[3] J. R. Morris, C. I. Contescu, M. F. Chisholm, V. R. Cooper, J. Guo, L. He, Y. Ihm, E. Mamontov, Y. B. Melnichenko, R. Olsen, S. J. Pennycook, M. B. Stone, H. Zhang, N. C. Gallego, *J Mater. Chem. A* **2013**, *1*, 9341.
[4] A.-H. Lu, S. Dai, *J. Mater. Chem. A* **2013**, *1*, 9326.
[5] T. P. Fellinger, A. Thomas, J. Yuan, M. Antonietti, *Adv. Mater.* **2013**, *25*, 5838.
[6] J. Wang, I. Senkovska, M. Oschatz, M. R. Lohe, L. Borchardt, A. Heerwig, Q. Liu, S. Kaskel, *ACS Appl. Mater. Interfaces* **2013**, *5*, 3160.
[7] Y. Xia, R. Mokaya, G. S. Walker, Y. Zhu, *Adv. Energy Mater.* **2011**, *1*, 678.
[8] V. Presser, J. McDonough, S. H. Yeon, Y. Gogotsi, *Energy Environ. Sci.* **2011**, *4*, 3059.
[9] G.-P. Hao, W.-C. Li, D. Qian, A.-H. Lu, *Adv. Mater.* **2010**, *22*, 853.
[10] N. Q. Zhao, N. Wei, J. J. Li, Z. J. Qiao, J. Cui, F. He, *Chem. Eng. J.* **2005**, *115*, 133.
[11] X. J. Wang, Y. Wang, X. Wang, M. Liu, S. Q. Xia, D. Q. Yin, Y. L. Zhang, J. F. Zhao, *Chem. Eng. J.* **2011**, *174*, 326.
[12] J. S. Huang, B. G. Sumpter, V. Meunier, *Angew. Chem. Int. Ed.* **2008**, *47*, 520.
[13] L. Zhao, L. Z. Fan, M. Qi, Z. H. Guan, S. Qiao, M. Antonietti, M. M. Titirici, *Adv. Mater.* **2010**, *22*, 5202.
[14] J. Chmiola, G. Yushin, Y. Gogotsi, C. Portet, P. Simon, P. L. Taberna, *Science* **2006**, *313*, 1760.
[15] M. Sevilla, A. B. Fuertes, *Energy Environ. Sci.* **2011**, *4*, 1765.
[16] D.-H. Liu, Y. Guo, L.-H. Zhang, W.-C. Li, T. Sun, A.-H. Lu, *Small* **2013**, *9*, 3852.
[17] M. D. Hornbostel, J. Bao, G. Krishnan, A. Nagar, I. Jayaweera, T. Kobayashi, A. Sanjurjo, J. Sweeney, D. Carruthers, M. A. Petruska, L. Dubois, *Carbon* **2013**, *56*, 77.
[18] B. V. Babu, S. Gupta, *Adsorption* **2008**, *14*, 85.
[19] D. W. Wang, F. Li, M. Liu, G. Q. Lu, H. M. Cheng, *Angew. Chem. Int. Ed.* **2008**, *47*, 373.
[20] M. Y. Endo, J. Kim, H. Ohta, I. T. Inoue, T. Hayashi, Y. Nishimura, T. Maeda, M. S. Dresselhaus, *Carbon* **2002**, *40*, 2613.
[21] M. Sevilla, A. B. Fuertes, *ACS Nano* **2014**, *8*, 5069.
[22] G.-P. Hao, Z.-Y. Jin, Q. Sun, X.-Q. Zhang, J.-T. Zhang, A.-H. Lu, *Energy Environ Sci.* **2013**, *6*, 3740.
[23] Z.-Y. Jin, A.-H. Lu, X.-X. Xu, J.-T. Zhang, W.-C. Li, *Adv. Mater.* **2014**, *26*, 3700.
[24] G.-P. Hao, A.-H. Lu, W. Dong, Z.-Y. Jin, X.-Q. Zhang, J.-T. Zhang, W.-C. Li, *Adv. Energy Mater.* **2013**, *3*, 1421.
[25] V. Chandra, S. U. Yu, S. H. Kim, Y. S. Yoon, D. Y. Kim, A. H. Kwon, K. S. Kim, *Chem. Commun.* **2012**, *48*, 735.
[26] S. Wang, W.-C. Li, G.-P. Hao, Y. Hao, Q. Sun, X.-Q. Zhang, A.-H. Lu, *J. Am. Chem. Soc.* **2011**, *133*, 15304.
[27] A.-H. Lu, T. Sun, W.-C. Li, Q. Sun, F. Han, D.-H. Liu, Y. Guo, *Angew. Chem. Int. Ed.* **2011**, *50*, 11765.
[28] A.-H. Lu, W.-C. Li, G.-P. Hao, B. Spliethoff, H. J. Bongard, B. B. Schaack, F. Schüth, *Angew. Chem. Int. Ed.* **2010**, *49*, 1615.
[29] J.-T. Zhang, Z.-Y. Jin, W.-C. Li, W. Dong, A.-H. Lu, *J. Mater. Chem. A* **2013**, *1*, 13139.
[30] J. An, S. J. Geib, N. L. Rosi, *J. Am. Chem. Soc.* **2010**, *132*, 38.
[31] M. Sevilla, P. V. Vigón, A. B. Fuertes, *Adv. Funct. Mater.* **2011**, *21*, 2781.
[32] Y. Xia, R. Mokaya, G. S. Walker, Y. Zhu, *Adv. Energy Mater.* **2011**, *1*, 678.
[33] B. Li, Z. Zhang, Y. Li, K. Yao, Y. Zhu, Z. Deng, F. Yang, X. Zhou, G. Li, H. Wu, N. Nijem, Y. J. Chabal, Z. Lai, Y. Han, Z. Shi, S. Feng, J. Li, *Angew. Chem. Int. Ed.* **2012**, *51*, 1412.
[34] S. R. Caskey, A. G. Wong-Foy, A. J. Matzger, *J. Am. Chem. Soc.* **2008**, *130*, 10870.
[35] L.-H. Zhang, Q. Sun, D.-H. Liu, A.-H. Lu, *J. Mater. Chem. A* **2013**, *1*, 9477.
[36] W. S. Hummers, R. E. Offeman, *J. Am. Chem. Soc.* **1958**, *80*, 1339.

Received: June 14, 2015
Published online: July 20, 2015